

Numerical Heat Transfer, Part A: Applications

An International Journal of Computation and Methodology

ISSN: 1040-7782 (Print) 1521-0634 (Online) Journal homepage: <http://www.tandfonline.com/loi/unht20>

Simulation of Slag-Skin Formation in Electroslag Remelting Using a Volume-of-Fluid Method

Jeffrey Yanke , Kyle Fezi , Rodney W. Trice & Matthew John M. Krane

To cite this article: Jeffrey Yanke , Kyle Fezi , Rodney W. Trice & Matthew John M. Krane (2015) Simulation of Slag-Skin Formation in Electroslag Remelting Using a Volume-of-Fluid Method, Numerical Heat Transfer, Part A: Applications, 67:3, 268-292, DOI: [10.1080/10407782.2014.937208](https://doi.org/10.1080/10407782.2014.937208)

To link to this article: <http://dx.doi.org/10.1080/10407782.2014.937208>



Published online: 23 Oct 2014.



Submit your article to this journal [↗](#)



Article views: 119



View related articles [↗](#)



View Crossmark data [↗](#)



Citing articles: 2 View citing articles [↗](#)

SIMULATION OF SLAG-SKIN FORMATION IN ELECTROSLAG REMELTING USING A VOLUME-OF-FLUID METHOD

**Jeffrey Yanke^{1,2}, Kyle Fezi¹, Rodney W. Trice¹, and
Matthew John M. Krane¹**

¹*School of Materials Engineering, Purdue Center for Metal Casting
Research, Purdue University, West Lafayette, IN, USA*

²*Carpenter Technology Corporation, Reading, PA, USA*

A modified volume-of-fluid method is implemented in a fixed-grid, finite-volume model simulating transport phenomena, solidification, and electromagnetics. The VOF model agrees well with published results, and the complete model is used to investigate process variations in the electroslag remelting process, in which liquid metal is melted from a consumable electrode immersed in an electrically resistive slag. The molten metal sinks through the slag cap floating on the liquid metal pool while a slag skin freezes to the mold. Here a VOF tracks slag skin formation and its effects on melt rate with different current levels and ingot diameters.

1. INTRODUCTION

Electroslag remelting (ESR) produces secondary ingots of specialty steels and superalloys by passing an electrical current through an electrode in contact with an electrically resistive slag, with Joule heating in the slag providing sufficient energy to melt the electrode. Droplets of melted electrode sink through the slag forming a pool of metal. Heat loss to the mold solidifies the metal, and the liquid pool is only 1–2 diameters deep throughout the process. A schematic is found in Figure 1. Slag also freezes on the mold, forming a skin. Thin skins tend to have a smooth finish, but thicker slag skins can be a source of surface defects causing severe grinding losses from the finished product [1, 2]. Understanding the mechanisms of skin formation in ESR is important for defect control and predicting the heat loss to the mold. While a much cheaper method than plant trials of understanding how process conditions affect slag skin growth, simulation of ESR presents challenges as it couples fluid flow, heat and mass transfer, solidification, and electromagnetics in both the metal and slag. A comprehensive model must include a method of tracking the slag–metal interface, and modified discretization techniques for the transport equations to account for property differences between the fluids.

Received 5 December 2013; accepted 3 May 2014.

Address correspondence to Prof. Matthew Krane, School of Materials Engineering, 701 West Stadium Ave., Purdue University, West Lafayette, IN 47907, USA. E-mail: krane@purdue.edu

Color versions of one or more of the figures in the article can be found online at www.tandfonline.com/unht.

NOMENCLATURE

A	Area	u	Radial velocity component
C	Composition	U	Overall heat transfer coefficient
c	Specific heat	V	Volume
D	Diameter	v	Axial velocity component
F	Fluid volume fraction	γ	Line constant
f	Phase mass fraction	Γ	Diffusion coefficient
G	Ratio of fluid volume fluxed to total fluxed volume across a face	μ	Viscosity
g	Phase volume fraction	μ_0	Permittivity of free space
h	Enthalpy	ρ	Density
H	Magnetic field	ξ	Ratio of final droplet diameter to initial diameter
j	Electrical current density	ω	AC frequency
k	Thermal conductivity		
K	Permeability	Subscripts	
\dot{m}	Melt rate	CV	Control volume
n	Surface normal	el	Electrode
\tilde{Q}	Total volume fluxed across a face	f	Fusion
q''	Heat flux	L	Liquid
S	Source term	rad	Radiation
T	Temperature	S	Solid

Several models have shown how processing variations affect ESR while simulating both the metal and slag regions. The first studies on the fluid behavior of slag and metal were by Dilwari and Szekely [3]. The flow was driven only by the electromagnetic force field induced by the current through the system. Heat transfer and thermal buoyancy were added to the model [4], and melting rates were predicted. Choudhary and Szekely [5] calculated pool profiles, and favorable comparisons were

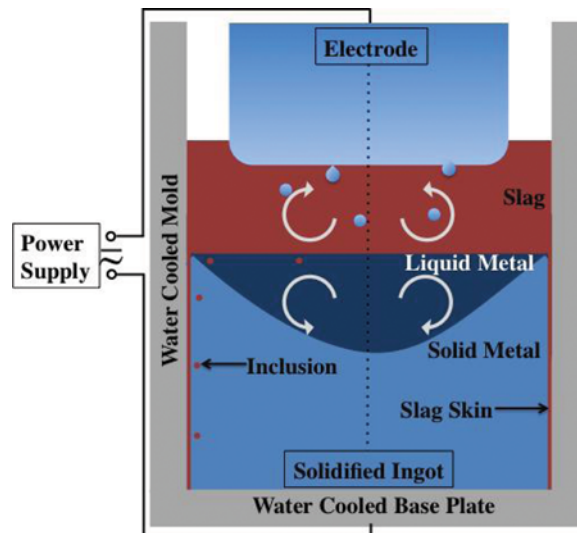


Figure 1. A schematic of an ESR furnace showing the general configuration of components [2].

made to laboratory-scale temperature measurements [5] and to industrial-scale temperature, pool profile, and power consumption data [6]. Good agreement of the predicted flow patterns to a lab-scale ESR simulator using mercury [7] was also found. Predicted temperatures in simplified flow fields were found to have reasonable agreement with experiments, but relied on several adjustable model parameters [8, 9]. All of these studies also made restrictive assumptions about the fluid flow between the mushy zone and the melt region.

Later numerical studies used single-domain models with one set of transport and electromagnetic equations in a unified numerical domain and improved predictions of pool shape as a function of melt rate and process current [8]. The effect of ingot radius and current on velocity and temperature was studied using numerical and scaling analysis [9]. Bertram et al. reported melt pool and flow predictions in the slag and the melt. Agreement with experimental pool shapes for an alloy 625 ingot did not show improvement from previous models [10]. Kelkar et al. [11] developed a steady-state, axisymmetric model including both metal and slag with a flat interface between them. This model compared computed sump shapes to pool markings in simulated industrial ESR processes. Patel and Kelkar used this model [12] to simulate microstructural characteristics with different alloys and process conditions.

A transient ESR model with a flat slag–metal interface was developed by Weber et al. [13], who used it to simulate a full experimental ESR run with changing process and found good agreement with predicted sump shapes. Using melt rate information from the experiments, they showed the variation of the Joule heating distribution in the slag with fill ratio, leading to an increase in melt rate with an increase in fill ratio. This model also predicted slag skin thickness [14] in the slag cap as a function of process parameters and material properties. The frozen slag skin in the real system results in a thinner slag cap as the process progresses, but Weber's model assumed a constant cap thickness.

Kharicha et al. developed an axisymmetric ESR model tracking a nonflat slag–metal interface, showing the effects of its motion on the electromagnetic fields in ESR [15]. The curved interface changed the ingot sump shape and Joule heating distribution in the slag. They [16] simulated electrode melting into a 3D slag layer, studying droplet formation and movement through the slag and finding the origins of metal droplets were not axisymmetric and they caused 1–2 cm-high waves in the slag–metal interface.

The present work develops an axisymmetric, transient model of ESR simulating fluid flow, heat and mass transfer, solidification, and electromagnetics. This model is coupled to a 1D conduction and electrode melting model to predict melt rates, and includes formation and remelting of slag skin. To predict the formation of solid slag and slag–metal interface motion, a volume-of-fluid (VOF) method was adapted from the literature for an axisymmetric domain.

VOF methods have been used extensively to study various processes ranging from microscale droplet deposition [17] to industrial-scale metal processing [16]. VOF calculates the volume fraction of each fluid in every cell on a fixed grid and uses these values to predict a sharp fluid boundary undergoing significant interface deformation. Hirt and Nichols [18] first used VOF to track the boundary of one fluid to determine where to apply boundary conditions internal to their numerical domain.

They devised rules for motion of fluid between cells (the donor–acceptor method) and assumed the interface could only be oriented with the orthogonal grid. However, the transport of VOF between cells using standard discretization of the advection equation causes the interface to smear over several control volumes. More recent versions [19, 20] used a geometric discretization of the VOF transport equation, relying on reconstruction of the fluid interface as a piecewise linear function and calculating the volume moved from one cell to another based on the face velocity and the reconstructed interface. These methods maintain a sharp interface without the use of higher-order advection discretization schemes and have the advantage of a convenient way to interpolate properties based on the reconstruction of the interface in each cell. The present ESR process model uses ideas from these methods to track the slag–metal interface.

2. MODEL DESCRIPTION

2.1. VOF Method

In this work, a VOF method is used to track the slag–metal interface in ESR. VOF methods [18, 20–24] track the fraction of a cell area (or volume in 3D) occupied by the tracked material, which is calculated and stored at the nodes in each control volume. This volume fraction is defined as

$$F = V_1/V_{CV} \quad (1)$$

If $F = 1$, the cell is all material 1; if $F = 0$, the cell is all material 2. Cells with $0 < F < 1$ contain the fluid–fluid interface. A VOF method consists of two main components: reconstruction from F of a subgrid level representation of the interface in each computational cell and advection of F between cells.

2.1.1. Treatment of interface. This work uses the method of Rider and Kothe to reconstruct a sharp subgrid interface from the VOF field [19]. Their technique involves a piecewise linear interface construction of the surface in each cell using a line defined with the surface normal:

$$xn_x + yn_y + \gamma = 0 \quad (2)$$

The first step in finding the surface normal is to locate the center of mass of material 1 in a 3×3 cell neighborhood around the interface cell. The first estimate of the direction of the surface normal is the direction of the line connecting the center of mass to the center of the interface cell. With this initial guess for all the surface normals and the line segments in each cell in the 3×3 neighborhood, lines are drawn from the line segment centers to the cell of interest, and a weighted average of these lines' surface normals is used to calculate the refined surface normal in the cell of interest.

The line constant, γ , is found from the line normal and the interface cell VOF using Brent's root finding algorithm [25] to solve

$$F(\gamma) - F = 0 \quad (3)$$

where $F(\gamma)$ is the area under the guessed interface and is calculated from area of polygons under the line, using the positions of the (m) vertices in Cartesian or axisymmetric coordinates [26]:

$$A_{\text{Cart}} = \frac{1}{2} \sum_{\nu=1}^m (x_{\nu} y_{\nu+1} - x_{\nu+1} y_{\nu}) \quad (4)$$

$$A_{\text{Axi}} = \frac{1}{6} \sum_{\nu=1}^m (r_{\nu} + r_{\nu+1})(r_{\nu} z_{\nu+1} - r_{\nu+1} z_{\nu}) \quad (5)$$

2.1.2. Advection of VOF. The method of VOF advection by Garrioch et al. [27] is modified here for axisymmetric coordinates. The VOF conservation equation is written as

$$\frac{\partial F}{\partial t} + \nabla \cdot (\bar{\mathbf{V}}F) = 0. \quad (6)$$

A special geometric discretization is used for the advection terms of this equation because algebraic discretizations smear the interface. Figure 2a shows an example of the geometric construction used to calculate the amount of material moving across the north face of a Cartesian control volume. This amount is equal to the product of the distance, $v_n dt$, and the control volume face area, A_n , but that volume does not originate just from directly below the interface. Some material is swept downstream by the horizontal velocities (u_w , u_e), to account for which Garrioch et al. [27] used an average transverse velocity, $u^* = (u_w + u_e)/2$. Using u^* , the volume swept across the face was equal to the volume predicted from the discretization, $v_n A_n dt$. Garrioch's discretization was in Cartesian coordinates and only works if the areas of the east and west control volume faces are the same. Figure 2b shows the swept volume crossing the top face of an axisymmetric cell, where a swept volume with parallel opposite sides (as in Figure 2a) will not conserve VOF. One of the two transverse offset distances, R^* , must be modified and can be calculated by setting equal the volumes A–B–C and D–E–F in Figure 2c, and rearranging to obtain

$$R_e^2 + r_e R_e + 2r_w^2 - 2r_e^2 - R_w^2 - r_w R_w = 0 \quad (7)$$

where all quantities are shown in Figure 2c. The transverse velocity, u^* , is calculated as in Garrioch's method and used to find R_w . Equation (7) is then solved for the one positive root of R_e . This procedure ensures that the volume of the fluxed material is equal to the discretized value, conserving VOF. In addition to calculating the total volume being swept across a control volume face, the amount of each material present in the swept volume must be calculated. Figure 3 shows a possible interface reconstruction, where the shaded region represents the fluid being tracked. The volumes of material leaving the control volume at the north and east faces are represented by the volumes A–B–C and G–H–I–J, respectively. The ratios of tracked material (G_e and G_n) leaving a control volume from the east and north interfaces to the total volume are used in the discretized advection terms of Eq. (6) instead of F .

$$G_e = GHIJ/EFHI \quad \text{and} \quad G_n = ABC/ABDE \quad (8)$$

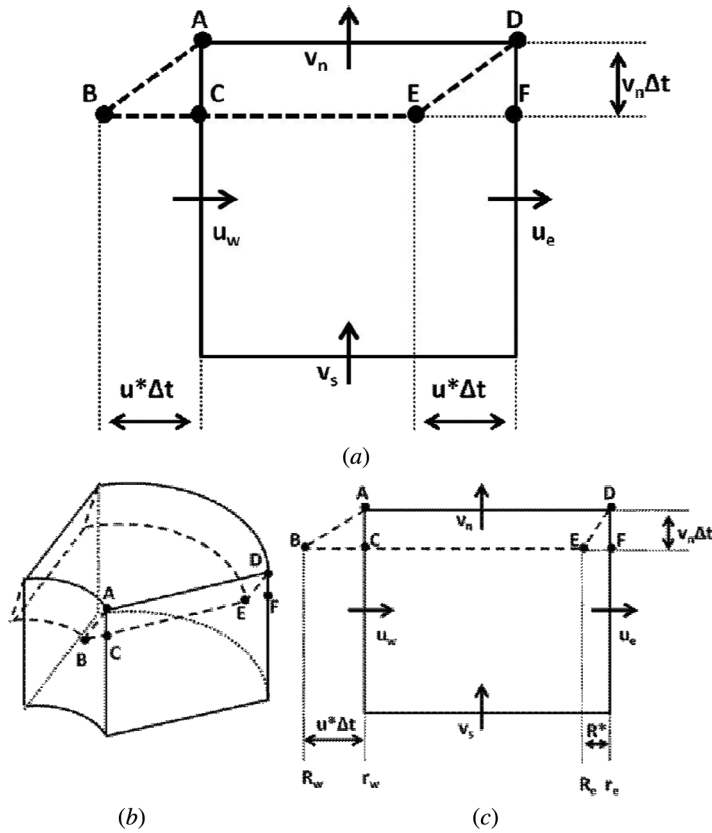


Figure 2. Geometric constructions used to calculate the fluid moving across control volume interfaces. The swept volumes are outlined by the dotted lines. (a) Construction for the north control volume face, where $u^* = (u_w + u_e)/2$. Using $u^* \Delta t$ as the offset distance at both the east and west faces leads to the volumes A-B-C and D-E-F being equal in Cartesian coordinates. (b) Different vertical control volume face areas on an axisymmetric grid are shown for Garrioch's method. (c) Side view of (b) showing that in order to make volumes A-B-C and D-E-F equal, the distance R^* and $u^* \Delta t$ must be different due to the difference in control volume face areas.

This substitution gives the final version of discretized VOF conservation equation,

$$(F - F^{old})V_{CV} + (Q_e)(G_e) - (Q_w)(G_w) + (Q_n)(G_n) - (Q_s)(G_s) = 0 \quad (9)$$

where $Q_i = u_i A_i \Delta t$ is the total volume swept across the face i .

This geometrical construction imposes a restriction on the ratio of grid spacing and time step,

$$v_i < \Delta x / \Delta t, \quad (10)$$

limiting the volume of material moved across a face in a given time step so that it does not overlap the swept material from adjacent control volumes. In practice, the volume being swept across a face in one time step should be less than 10% of

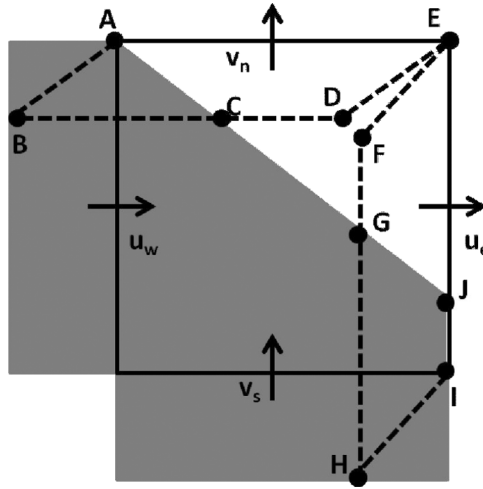


Figure 3. A schematic of the swept volumes across the east and north faces, with the shaded region representing the fluid being tracked. The volume of tracked material passing across the north and east faces is given by A–B–C and G–H–I–J, respectively.

the volume of the control volume for a stable solution. This limit applies not just to interface cells, but everywhere in the domain.

2.2. Conservation Equations

Following the procedure of Bennon and Incropera [28], all transport variables for fluid j are written as mixture quantities, ϕ_j , weighted by the phase mass fraction,

$$\phi_j = f_s \phi_s + (1 - f_s) \phi_{s'}, \quad \text{where } \phi_j = \bar{V}_j, h_j, \text{ or } C_j^i \quad (11)$$

or by the phase volume fraction,

$$\phi_j = g_s \phi_s + (1 - g_s) \phi_{s'}, \quad \text{where } \phi_j = \rho_j \text{ or } k_j. \quad (12)$$

The conservation equations for heat, mass, momentum, and species are written in terms of the individual phases, the equations are summed over all phases, and then rearranged into the standard advection–diffusion form for the mixture quantities, ϕ_j :

$$\frac{\partial}{\partial t} (\rho_j \phi_j) + \nabla \cdot (\rho_j \bar{V} \phi_j) = \nabla \cdot (\Gamma \nabla \phi_j) + S_\phi \quad (13)$$

A set of mixture conservation equations in this form are found for each of the two fluids, and the final set is found by adding equations of the two fluids together, weighted by volume of fluid:

$$\phi = F \phi_1 + (1 - F) \phi_2 \quad (14)$$

This procedure allows for one set of conservation equations to be solved in the computational domain, over all phases in both fluids.

2.2.1. Momentum conservation. The momentum conservation equations are derived assuming that the solid phase is stationary:

$$\frac{\partial(\rho u)}{\partial t} + \nabla \cdot (\rho \bar{V} u) = \nabla \cdot (\mu \nabla u) - \frac{\partial P}{\partial x} - \frac{\mu}{K} u - \mu_{ax} H_{\theta} \quad (15)$$

$$\begin{aligned} \frac{\partial(\rho v)}{\partial t} + \nabla \cdot (\rho \bar{V} v) = & \nabla \cdot (\mu \nabla v) - \frac{\partial P}{\partial y} - \frac{\mu}{K} v - \mu_{ay} H_{\theta} \\ & - g \rho \left[\beta_T (T - T_o) + \sum_1^{N-1} \beta_S^i (C_L^i - C_{L,o}^i) \right] \end{aligned} \quad (16)$$

The source terms are due to drag in a porous medium and the Lorentz force, and, in the z -direction, to the thermal and solutal buoyancy in an N -component alloy. The permeability of the mushy zone needed to model the drag is represented here by the Blake–Kozeny equation [28].

2.2.2. Mass continuity. In most mixture conservation equations, the two-fluid VOF method does not affect their numerical treatment, except in the calculation of thermophysical properties (see below). Continuity does require special treatment due to the large density differences that may exist across the sharp interface. In this model, the metal and slag are incompressible, but their mixture in interface cells is not, as seen in Eq. (14) with $\phi = \rho$. The SIMPLER algorithm used here to solve for pressure and flow fields is designed for an incompressible fluid and does not work well for fluids with large variations in density.

The conservative form of the continuity equation is

$$\frac{\partial \rho}{\partial t} + \nabla \cdot \rho \bar{V} = 0 \quad (17)$$

By substituting the definition of mixture density, Eq. (14), and applying the chain rule, we get

$$(\rho_1 - \rho_2) \left(\frac{\partial F}{\partial t} + \bar{V} \cdot \nabla F \right) + [F \rho_1 + (1 - F) \rho_2] (\nabla \cdot \bar{V}) = 0 \quad (18)$$

Recognizing that the first term is identically zero from the VOF Eq. (6), all that remains is incompressible continuity equation,

$$\nabla \cdot \bar{V} = 0 \quad (19)$$

This form of the continuity equation can be thought of as a “volume conservation” and this elimination of density also removes it from the pressure and pressure correction equations in the SIMPLER algorithm.

2.2.3. Energy and species conservation. The energy equation used here is in terms of mixture enthalpy, as in Bennon and Incropera [28],

$$\frac{\partial(\rho h)}{\partial t} + \nabla \cdot (\rho \bar{V} h) = \nabla \cdot \left(\frac{k}{c} \nabla h \right) + \nabla \cdot \left(\frac{k}{c} \nabla (h_s - h) \right) - \nabla \cdot (\rho \bar{V} \nabla (h_s - h)) + \frac{1}{2\sigma} \text{Re}(\bar{j} \cdot \bar{j}) \quad (20)$$

The last term is Joule heating, which is calculated using the current density from the solution of the AC electromagnetics. The origin of the diffusion-like and advection-like source terms is discussed in Ref. [28].

Upwind differencing is used in the advection terms and, while this discretization works inside each of the two fluids, a false heat generation was found in interface cells where the two fluids have different specific heats. Figure 4 shows an example of how this error occurs. Upwinding the nodal value of enthalpy (averaged over the cell) to the cell faces incorrectly assumes that what leaves the control volume is the mixture of materials contained in the entire cell. The solution to this problem is to treat the values of advected enthalpy as a mixture of the material actually crossing the control volume face, a quantity calculated from the VOF advection algorithm, as

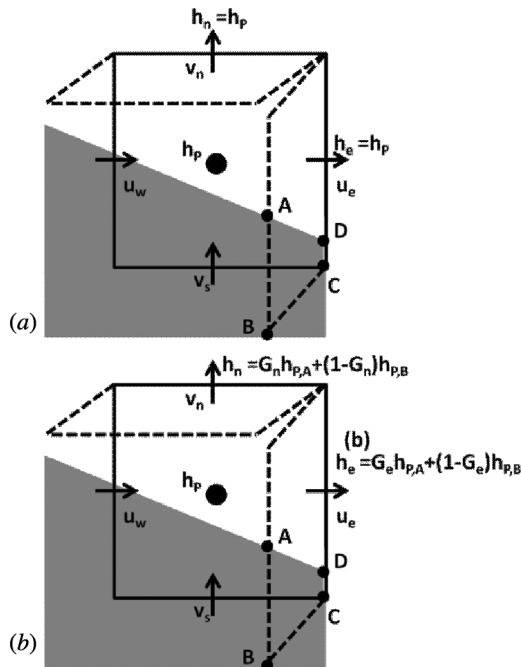


Figure 4. A schematic of interface control volumes showing the value of the enthalpy advected across the north and east control volume faces. (a) The upwind method assigns the same nodal enthalpy value to north and east enthalpies, even though different fractions of material are crossing the faces. (b) Enthalpies advected across the north and east faces calculated as the volume-averaged mixtures of the fluids actually moving across each face.

shown in Figure 4b. Davidson and Rudman [29] use a similar method to correct errors introduced by upwinding enthalpy values in their method, which treated each fluid separately and linked them together with source terms.

As with the energy equation, species conservation is written in terms of a mixture quantity:

$$\frac{\partial(\rho C^i)}{\partial t} + \nabla \cdot (\rho \bar{V} C^i) = \nabla \cdot (D \nabla C^i) + \nabla \cdot (D \nabla (C_L^i - C^i)) - \nabla \cdot (\rho \bar{V} (C_L^i - C^i)) \quad (21)$$

where i denotes the species of interest. In the present work, alloy 718 is approximated by five elements (Ni, Fe, Cr, Nb, and Ti), which were selected because they have the largest influence on the alloy freezing range. Transport of species varies in the metal, while slag composition is treated as uniform and constant.

2.2.4. Calculation of properties. The utility of the VOF method is its ability to track the motion of a sharp interface between two fluids with large property differences. An important part of this method is the proper calculation of properties for the three types of terms found in general advection–diffusion equation: volumetric, diffusion, and advection. Properties appearing in the volumetric terms are found from a simple volume average:

$$\theta_{\text{Volumetric}} = F\theta_A + (1 - F)\theta_B \quad (22)$$

where θ represents a generic thermophysical property of fluids 1 and 2. The other two types of terms represent surface effects and the properties are needed at the cell faces. For the diffusion terms, the properties are found using a harmonic mean of the mixture nodal values of the two cells [30]. The advection terms model the transport of a quantity across a control volume face by fluid motion in a similar way as the VOF transport in Figure 2. This concept is used to calculate properties in advection equations using the fraction of tracked material moving across a control volume face:

$$\theta_{\text{Advection:fc}} = G_{fc}\theta_A + (1 - G_{fc})\theta_B \quad (23)$$

Calculating advection properties at the control volume faces removes interpolation errors that can occur with large variations in properties [31].

The exception to these procedures is the momentum equations which are on a staggered grid, shown in Figure 5. The u control volume's east and west faces lie at the center of the main control volumes. Because VOF is stored and reconstructed on the main control volumes, no fluxing information is available at these faces for the staggered control volume. Instead, the fraction of the interface containing tracked fluid (the distance $AB/\Delta y$) is used in place of G in Eq. (23). Similar treatment is done for the v -staggered control volumes.

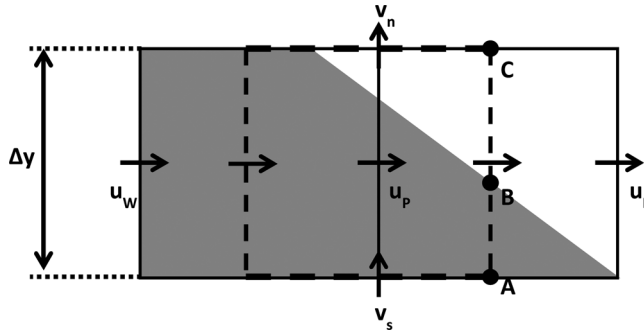


Figure 5. The geometry on a staggered grid of a u velocity control volume, outlined by dashed lines. The tracked fluid ($F=1$) is the shaded region. Advected properties at the east and west faces of the u control volume are calculated as weighted fractions, using $AB/\Delta y$.

2.3. Solidification

The solidification model is based on Bennon and Incropera [32], in which the mixture enthalpy and composition (h and C^i) are known in each control volume from solution to the transport equations and are used to find temperature, phase fractions, and phase compositions. In this work, the slag is treated as a pure substance that freezes at a single temperature and the metal is a multicomponent alloy with primary phase solidification followed by an isothermal reaction if necessary.

Assuming that the solid and liquid slag have the same specific heat, the enthalpies of the solid and liquid at the isothermal melting temperature are

$$h_{\text{SOL}} = c_p T \quad (f_S = 1) \quad \text{and} \quad h_{\text{LIQ}} = c_p T + h_f \quad (f_S = 0).$$

If $h \geq h_{\text{LIQ}}$, then

$$T = (h - h_f)/c_p \quad \text{and} \quad f_S = 0$$

and if $h \leq h_{\text{SOL}}$, then

$$T = h/c_p \quad \text{and} \quad f_S = 1.$$

At the melting temperature ($T = T_m$), $h_{\text{SOL}} < h < h_{\text{LIQ}}$ and

$$f_S = (c_p T_m + h_f - h)/h_f.$$

The metal alloy freezes over a temperature range defined by the equilibrium phase diagram. For the calculation of the primary solidification behavior in this range, commercial software (PANDAT) was used to predict the liquidus surface for a Ni-Fe-Cr-Nb-Ti alloy as an approximation of alloy 718:

$$T_{\text{LIQ}} = 1728 - 6.21 C_L^{\text{Fe}} - 292.5 C_L^{\text{Cr}} - 1253.6 C_L^{\text{Nb}} - 1872.6 C_L^{\text{Ti}} \quad (T \text{ in K}) \quad (24)$$

The software also provided the partition coefficients found in Table 1. Given the mixture enthalpy and composition, the state of the metal (all liquid, primary

Table 1. Thermophysical properties for alloy 718 and slag [1] used in the simulations

	Metal	Slag		Metal	Slag
ρ [kg/m ³]	7500	2490	k^{Fe} [-]	1.3	—
c_p [J/kg K]	720	1260	k^{Cr} [-]	1.2	—
k [W/m K]	30.52	6	k^{Nb} [-]	0.3	—
μ [kg/ms]	0.0033	0.025	k^{Ti} [-]	0.4	—
β_T [1/K]	0.00015	0.00025	D_L [m ² /s]	1.0E-09	1.0E-09
ε	—	0.87	h_f [J/kg] [8]	2.1E+05	4.75E+05
β_S^{Fe} [-]	0.124	—	T_{eut} [K]	1411	1390
β_S^{Cr} [-]	0.206	—	σ [1/Ωm]	7.1E+05	Variable
β_S^{Nb} [-]	0.041	—	Metal film	0.006	—
β_S^{Ti} [-]	0.528	—	Thickness [m]		
C_o^{Fe} (wt%)	18.4	—	C_o^{Nb} (wt%)	5.02	—
C_o^{Cr} (wt%)	18.0	—	C_o^{Ni} (wt%)	Bal.	—
C_o^{Ti} (wt%)	1.04	—			

solidification, eutectic solidification, or all solid) is determined assuming thermodynamic equilibrium. The solution method for fraction solid, temperature, and solid and liquid compositions is the same as in Ref. [32], except in primary solidification. Using the liquidus surface (24) and the definitions of partition coefficient ($k^i = C_S^i/C_L^i$) and mixture composition, and guessing f_S from the previous iteration of the transport equations, a bisection search for f_S is performed until the calculated mixture enthalpy is within $10^{-3}\%$ of the value from Eq. (20).

The solidification models that are discussed above assume a single fluid in a control volume. The modifications required to include two fluids in the same cell are straightforward when the fluids' freezing ranges do not overlap. The mixture enthalpy and fraction solid can be written as

$$h = Fh_1 + (1 - F)h_2 \quad (25)$$

and

$$f_S = Ff_{S,1} + (1 - F)f_{S,2} \quad (26)$$

where h_1 and h_2 are the mixture enthalpies of fluids 1 and 2. The fluid-specific values are used in place of the mixture values in the above procedures to calculate temperature, fraction solid, and compositions.

2.4. Electromagnetics

The AC electromagnetics model for plant scale ESR can be greatly simplified by noting that the low magnetic Reynolds number indicates that only diffusion of magnetic field affects the electromagnetics. Additionally, assuming magnetic diffusion is fast enough that a quasistatic magnetic field exists leads to:

$$\nabla \cdot \left(\frac{1}{\sigma} \nabla \bar{H} \right) = j\omega\mu_o \bar{H} \quad (27)$$

where \vec{H} represents the azimuthal complex amplitude of the magnetic field. Equation (27) is divided into real and imaginary parts for magnetic diffusion. These equations are linked through the source terms on the right-hand side of Eq. (27). Current density is calculated from the magnetic field as

$$\nabla \times \vec{H} = j \quad (28)$$

and stored at the control volume faces, much like the velocities. Current density is used to calculate both the Joule heating in the energy equation and the Lorentz force in the momentum equations. Because the current density is calculated at the control volume faces, no alteration is required to compute the Lorentz force. However, a linear interpolation of the staggered current densities to the center of the control volumes is used to calculate the Joule heating source term.

3. VOF MODEL EVALUATION

3.1. Verification: Enthalpy Advection with Two Fluids

To illustrate the problem with standard upwinding and to test the efficacy of the proposed method of correction, a simple test case was developed. It consists of an axisymmetric domain initially at 1,800 K half full of metal and half full of slag, each with the thermophysical properties shown in Table 1. A constant and uniform axial velocity corresponding to a typical industrial ESR filling rate is imposed everywhere in the domain to simulate metal entering at the bottom and slag leaving at the top. The side walls are insulated, and the inlet and initial temperatures are the same (1,800 K), so the whole domain should have a constant and uniform temperature as the metal/slag interface passes through the domain.

The effect of the upwind differencing in the interface cell when fluids have different specific heats is seen in Figure 6. Figure 6a shows that upwinding causes large temperature deviations with pure advection, ranging from a 244 K rise on the metal side of the interface to a 320 K decrease in the slag. The VOF-based method of calculating enthalpy advection shows significantly less deviation, with only a 1.6 K increase in temperature in the interface cell. Figure 6b shows the same test case run with both advection and diffusion, where both have less deviation than without diffusion, but the error with the upwinding is still unacceptably high. Basing enthalpy advection on volumes of fluid crossing the control volume face offers significant improvement over standard upwinding while adding little computational overhead as the pertinent quantities are already being calculated for the VOF advection equation.

3.2. Validation: Collapsing Dam

The purpose of the first validation of this two-fluid VOF confirms that interface tracking is working correctly with the fluid mechanics. To this end, a collapsing dam is simulated, in which an initially static column of fluid ($W_o = 2.86$ cm wide and $L_o = 5.72$ cm tall) is allowed to fall under gravity. A time step and grid dependence study was performed and convergence was found with a uniform grid spacing of

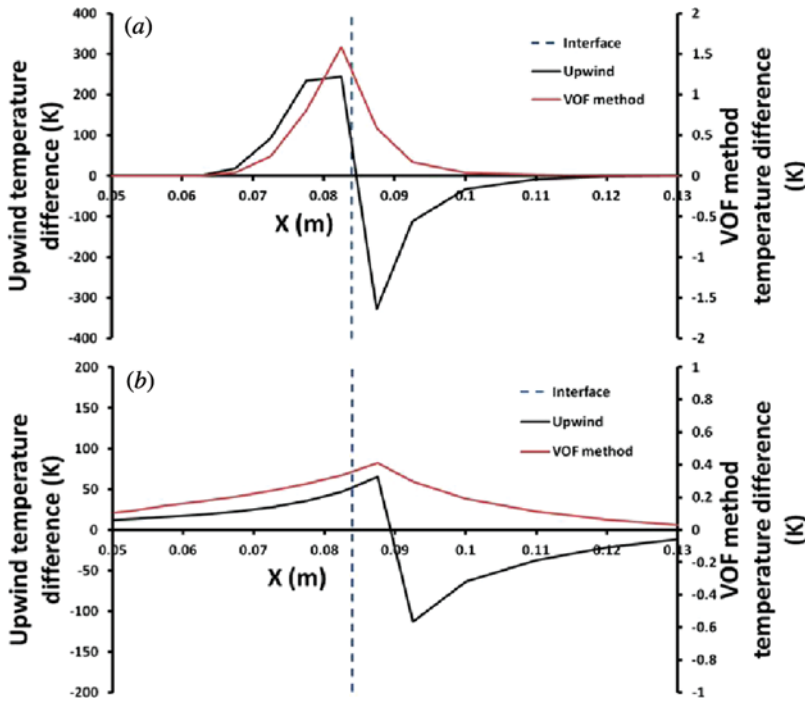


Figure 6. Plots of temperature deviation ($T-1,800\text{ K}$) near a moving metal–slag interface, where the domain is initially at $1,800\text{ K}$, showing much less change when the VOF method is used. Results from upwinding are associated with left vertical axes; those from the VOF method with right axes. (a) Temperature differences with only advection and (b) with advection and diffusion.

0.7 mm and time step of 10^{-4} s . The predicted transient surge front position is compared to the experiments of Martin and Moyce [33]. The nondimensional surge front position, X^* , as a function of time is defined by

$$X^* = \frac{x}{W_o} \text{ and } T^* = t \left(\frac{gL_o}{W_o^2} \right)^{1/2} \quad (29)$$

In Figure 7a, the simulation shows excellent agreement with the experiment.

3.3. Validation: Yttria-Stabilized Zirconia Droplet Impact and Solidification

The algorithm for predicting interface motion and fluid flow was linked to the solidification and heat transfer models, and simulation results were compared to the experiments on Yttria-stabilized zirconia (YSZ) droplet deposition of Shinoda et al. [34]. In these simulations, liquid droplets with $100\text{ }\mu\text{m}$ diameter impacted a cold copper substrate, with an assumed contact resistance between it and the droplet, and flatten out as they freeze on the substrate. Heat transfer was calculated only in the

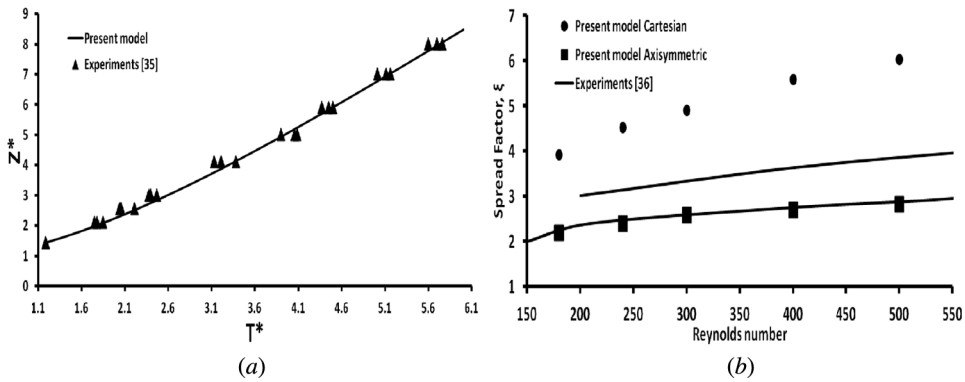


Figure 7. Comparison of numerical algorithm with experimental results. (a) Nondimensional surge front position for a collapsing dam as a function of nondimensional time, comparing the experiment of Martin and Moyce [33] to the simulation. (b) Spreading factor for liquid YSZ droplets as a function of Reynolds number, comparing the present model in axisymmetric and Cartesian coordinates to the experimental bounds of Shinoda et al. [34].

YSZ droplet. Simulations were run at different droplet Reynolds numbers and in an axisymmetric coordinate system.

Madjeski [35] analyzed a flattening droplet with friction and surface tension and found that for plasma processing parameters, the ratio of the final splat diameter to the initial droplet diameter, $\xi = D_f/D_o$, will only depend on the friction and initial momentum of the droplet, not the surface tension. Typically, this data is represented as a correlation between ξ and Reynolds number, $Re = \rho VD/\mu$, which under typical plasma spray conditions takes the form

$$\xi = C_1 Re^n. \quad (30)$$

A plot of $\xi = f(Re)$ is shown in Figure 7b, comparing the current model to Shinoda's experiments. The predictions tend to be at the low end of the range of experimental data, possibly due to the influence of solidification slowing the droplet spreading as it nears its maximum flattening ratio. The results show the current VOF method works with fluid mechanics and heat transfer in an axisymmetric coordinate system.

4. MODEL CONSIDERATIONS SPECIFIC TO THE ESR PROCESS

4.1. Mesh Refinement

The model of ESR process is used in an axisymmetric domain to simulate the casting of cylindrical ingots. To increase the computational efficiency, equations of fluid motion and species are only solved in a subdomain stretching from five control volumes below the $f_S = 1$ line to the top of the slag cap. The energy and magnetic field equations are solved over the entire domain.

A locally refined mesh was used in all ESR simulations (Figure 8). The unrefined grid size is 0.01 m in the axial direction and 0.0043 m in the radial. All mesh refinements reduce this mesh size by 50%. The mesh was refined in the axial direction within 0.02 m of the original slag/metal interface and in the 0.06 m under the

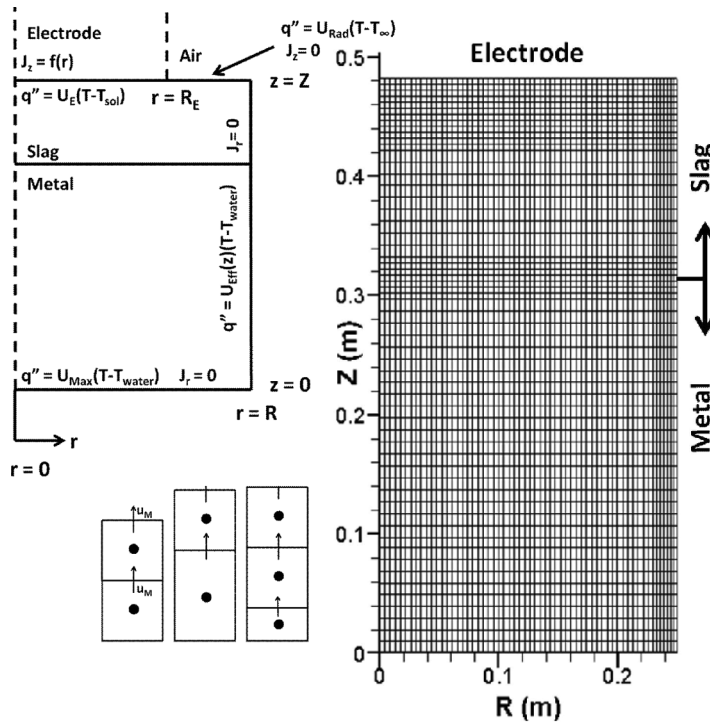


Figure 8. Computational mesh and electromagnetic and thermal boundary conditions used in ESR simulations. The mesh is refined in z -direction near the electrode and slag–metal interface and in r near the mold wall. The inset in the lower left corner illustrates the method of growing the domain using the moving mesh. As the bottom control volume becomes 1.5 times the original size, it is split into two control volumes, one of the original size and one half size.

electrode. The radial direction was refined in the 0.02 m between the edge of the electrode and mold wall. These refined regions are necessary as these areas in the ESR process are subjected large gradients in temperature and flow conditions.

4.2. Addition of Melted Electrode Material

The domain is bounded by the flat bottom of the electrode, which is in perfect contact with the top of the slag cap, and the interior mold walls. Kharicha et al. [16] have shown that metal droplets falling from the electrode are typically 0.01–0.02 m in diameter, which is too small to resolve accurately on a grid coarse enough to efficiently simulate on industrial-scale ingots. In this work, motion of metal melted from the electrode is not modeled through the slag, but is immediately transferred evenly across the slag–metal interface, with a temperature matching the metal at the interface and having the nominal alloy composition. This treatment is manifested as source terms in the energy, species, and mass conservation equations in slightly different forms. The energy source term due to mass addition is

$$S_{\text{mass}}^{\text{energy}} = \dot{m}_{\text{el}} h_{\text{metal}} / V_{\text{CV}} \tag{31}$$

The source term differs slightly for the species equations because the advection terms are discretized using the upwind method, which requires the continuity equation to be multiplied by ϕ_P and subtracted from the species equation. The source term must then account for both the addition of metal in the species equation and as another term from the continuity equation, taking the final form

$$S_{\text{mass}}^i = \dot{m}_{\text{el}}(C_o^i - C^i)/V_{CV} \quad (32)$$

which brings the composition of interface cells closer to the nominal composition, as expected when adding metal of nominal composition to a control volume. Due to the volumetric formulation of the continuity equation used in this work, the source term for the volume continuity equation is

$$S_{\text{mass}}^{\text{cont}} = \dot{m}_{\text{el}}/\rho_{\text{metal}}V_{CV}. \quad (32)$$

4.3. One-Dimensional Electrode Model

In order to calculate the electrode melt rate, \dot{m}_{el} , a separate one-dimensional heat conduction model was used to calculate the temperature profile in the electrode. The domain shrinks over time due to electrode melting, so the standard 1D transient conduction equation includes an advection term:

$$\frac{\partial(\rho c T)}{\partial t} - \frac{\partial(\rho c u_{\text{Mesh,electrode}})}{\partial z} = \frac{\partial}{\partial z} \left(k \frac{\partial T}{\partial z} \right), \quad (33)$$

where the electrode mesh velocity is

$$u_{\text{Mesh,electrode}} = \frac{\dot{m}}{\rho_{\text{Metal}}A_{C,\text{electrode}}}. \quad (34)$$

The moving mesh term is used so the domain can be pinned to the melting face of the electrode ($z=0$). The boundary condition at that face is a constant temperature, T_{SOL} , and there is a no-flux condition at the top of the electrode. Because the start-up of the process is not modeled, an initial temperature profile is calculated by running the electrode model with a constant heat flux of $7.0 \times 10^5 \text{ W/m}^2$ (similar to typical fluxes calculated during ESR simulation) for 10 min of process time. The temperature far from the slag is initially 300 K. The mesh spacing is 0.01 m, and the time step is the same as the main simulation.

An iterative procedure to split the slag heat flux is developed to calculate the melt rate. This heat flux (calculated from the slag temperature field) is absorbed by a combination of latent and sensible heats:

$$q''_{\text{Slag}} = q''_{\text{Latent}} + q''_{\text{Sensible}} \quad (35a)$$

$$q''_{\text{Latent}} = \frac{\dot{m}h_f}{A_{\text{Electrode}}} \quad \text{and} \quad q''_{\text{Sensible}} = -k \frac{\partial T}{\partial z} \Big|_{z=0, \text{Electrode}}. \quad (35b)$$

An initial guess of $q''_{\text{latent}} = 0.1 q''_{\text{sensible}}$ and the previous time steps' melt rate are used to solve Eq. (33) for the temperature field in the electrode. Using Eq. (35), the sensible heating in the electrode is calculated and used to find the latent heating and then the melt rate. Equation (33) is then solved again with the updated melt rate and this procedure is repeated until the sensible heating changes less than 1% in one iteration, and the temperature changes in all the control volumes are less than $10^{-4}\%$.

4.4. Moving Mesh

As mentioned above, the heat flux leaving the slag at the top of the domain is required to calculate the melt rate in the electrode model. Originally, a model tracked the VOF at the top of the slag cap, as it floated upwards through a fixed mesh. Attempts to calculate a heat flux out of this moving boundary were not successful as a severe dependence of the computed heat flux on the volume of fluid was observed. As a remedy, a moving mesh was developed, attached to the top of the slag cap so the position of the slag–electrode interface in the lab frame of reference will not affect the calculation of the heat flux leaving the slag. The mesh velocity is set equal to the filling velocity, defined by

$$u_{\text{mesh}} = u_{\text{fill}} = \frac{\dot{m}_{\text{el}}}{\rho_{\text{metal}} A_{\text{mold}}}. \quad (36)$$

The bottom of the domain remains stationary, and a control volume is designated as the boundary between the stationary portion of the domain and the moving portion. This control volume grows (as only the top control volume face is moving) until it reaches 1.5 times the nominal control volume size in the axial direction. Once this size is reached, the control volume is split into two control volumes as shown in Figure 8, one with a nominal size control volume and one half size control volume.

In all of the conservation equations, the axial velocity (u) is replaced with the term $(u - u_M)$ to account for the moving mesh, with the exception of the advection-like source term in the energy and species conservation equations. These terms only exist when there are two phases with different velocities present in a control volume. In this case, the portion of the advection-like source term that results from mesh velocity is zero due to the mesh velocity being equal for all phases.

4.5. Boundary Conditions

Figure 8 shows a schematic of the boundary conditions of a typical axisymmetric ESR system. The baseplate ($z=0$) and the mold ($r=R$) are water-cooled copper, and the top of the slag is either exposed to air (at higher radii) or in contact with the electrode. No-slip conditions are imposed on velocity at the mold ($r=R$), baseplate ($z=0$), and electrode ($z=z_{\text{top}}, r < R_E$), while a no shear condition is applied to the slag exposed to air ($z=z_{\text{top}}, r > R_E$) and a symmetry condition is used at $r=0$. The species equations have a no-flux condition on all boundaries. The electromagnetic boundary conditions assume a fully developed current profile at the

baseplate, $J_r(z=0)=0$, and no current leakage to the mold, $J_z(r=R)=0$, or the air, $J_r(z=z_{\text{top}})=0$. An analytical profile [36] for the current is assumed at the electrode/slag boundary.

The thermal boundary conditions in the computational domain are somewhat more complex. The baseplate has a single, overall heat transfer coefficient (h_{base}), representing the thermal resistance of the copper mold and the contact resistance between metal and mold. The values for this coefficient are difficult to determine because there is an unknown amount of slag frozen to the baseplate, and the contact area between baseplate and solidifying ingot is not known. However, this boundary condition has a diminishing effect on the ESR process as the solidifying metal front moves away from the bottom of the mold. In this work, it is assumed that the overall heat transfer coefficient acting on the bottom of the mold is the same as the overall heat transfer coefficient acting at the side walls, including resistance attributed to slag skin.

At the mold wall, the effective heat transfer coefficient used is a function of the axial position along the mold. There is a (higher) value used in the liquid regions, another (lower value) in the completely solid regions, and a linear interpolation between those two values, weighted by volume of frozen metal at that axial position, approximating the effect of increasing thermal resistance due to metal shrinkage as solidification progresses. The top thermal boundary condition ($z = z_{\text{top}}$) is more complicated. The heat loss to the air is treated by a linearized radiation condition:

$$q'' = U_{\text{rad}} * (T - T_{\text{air}}) \quad U_{\text{rad}} = (5.67 \times 10^{-8} \text{ W/m}^2 \text{ K}^4) * \varepsilon * (T + T_{\text{air}}) * (T^2 + T_{\text{air}}^2).$$

The exchange of heat between slag and electrode is found by coupling domain boundary ($z = z_{\text{top}}, r < R_c$) to the electrode heat transfer model described above. The boundary temperature between slag and electrode is set by considering the heat flux leaving the electrode, the solidus temperature of the electrode material, and a constant-thickness liquid metal film that exists between solid electrode and liquid slag. For all studies presented, this metal film is assumed to be uniformly 6 mm thick.

5. RESULTS AND DISCUSSION

5.1. Cases for the Parametric Study

In order to demonstrate the use of the VOF in ESR simulations, this model is used under a variety of different conditions similar to industrial practice and the effects of including slag skin formation are included. For all cases, properties for alloy 718 and a CaF_3 -15% CaO -15% Al_2O_3 slag were used, as in Table 1. The metal alloy properties are better known, but there is much more uncertainty in the slag data [1]. Initial conditions are identical for all cases, with 7 cm of liquid metal and a liquid slag cap, both at a uniform temperature of 1,700 K. Also, a 3 mm thick solid slag skin at 500 K was included at the mold wall. These conditions allowed a numerically stable start-up of the process and are a vast simplification of a “wet start”, in which the process is begun by adding liquid slag to beneath the electrode. (The more common “dry start” begins with striking an arc between the electrode and a pile of

solid slag and metal scrap, but the phenomena in that process are beyond the capabilities of the present model.)

The details of the four cases simulated are shown in Table 2. Cases 1–3 show the base case (Case 1) and the effects of increasing current density (Case 2) and ingot radius (Case 3) on slag skin thickness and liquid metal sump shape. The larger diameter (Case 3) requires a larger current to achieve stable melting conditions. Initially, the current densities were kept the same, scaling the current up from 13 to 28.9 kA. When Case 3 was run at 28.9 kA, the slag skin in the cap completely melted, and without the insulating slag skin, the heat lost to the mold was large enough to prevent any melting of the electrode. The current for Case 3 was determined through trial and error, and 25 kA was found to provide a stable melt rate without completely melting the slag skin. All cases are run at the constant currents (Table 2). Case 4 illustrates how the model behaves differently if, instead of predicting a variable slag skin, a constant thickness slag skin is assumed giving a constant overall thermal resistance at the mold wall.

5.2. Slag Skin Thickness and Liquid Sump Shape

Figure 9 shows a comparison of slag skin thickness and sump shape near the mold wall for cases 1–3 at 200 min into the process, at which time all the sump shapes are at steady state. For a constant diameter, increasing current density of $\sim 15\%$ decreases the slag skin thickness from 0.005 to 0.003 m, a trend in accord with industrial observations. This change also increases the sump depth at the centerline from 7.5 to 14 cm. The sump shape at lower current is shallower and bowl-shaped, whereas the higher power case shows a deeper “V”-shaped sump more common in ESR [37].

Similar trends can be seen in Cases 1 and 3. Case 3 shows the same slag skin thickness (0.003 m) and similar V-shaped sump as in Case 2. This similarity is explained by their similar filling velocities, which is used to compare cases of different diameter in which speed, not the melt rate, controls the shape of the sump. Filling velocity histories for Cases 1–4 (Figure 10a) show that Cases 2 and 3 are within $\sim 10\%$ of each other even though the current supplied to Case 3 is 67% higher than in Case 2. The larger melt rate produced by this higher current is offset by the larger volume (2.3 times the volume of Case 2) that Case 3 must fill to move the slag–metal interface. Both Cases 2 and 3 have filling velocities that are 60% higher than Case 1. This similarity in filling velocities between Cases 2 and 3 results in similarly shaped

Table 2. Process parameters

Case #	Current (kA)	Mold radius (m)	Electrode radius (m)	Maximum mold wall heat transfer coefficient ($\text{W}/\text{m}^2 \text{K}$)	Minimum mold wall heat transfer coefficient ($\text{W}/\text{m}^2 \text{K}$)
1	13	0.25	0.23	2,000	92
2	15	0.25	0.23	2,000	92
3	25	0.381	0.343	2,000	92
4	13	0.25	0.23	400 (includes constant and uniform slag skin)	92

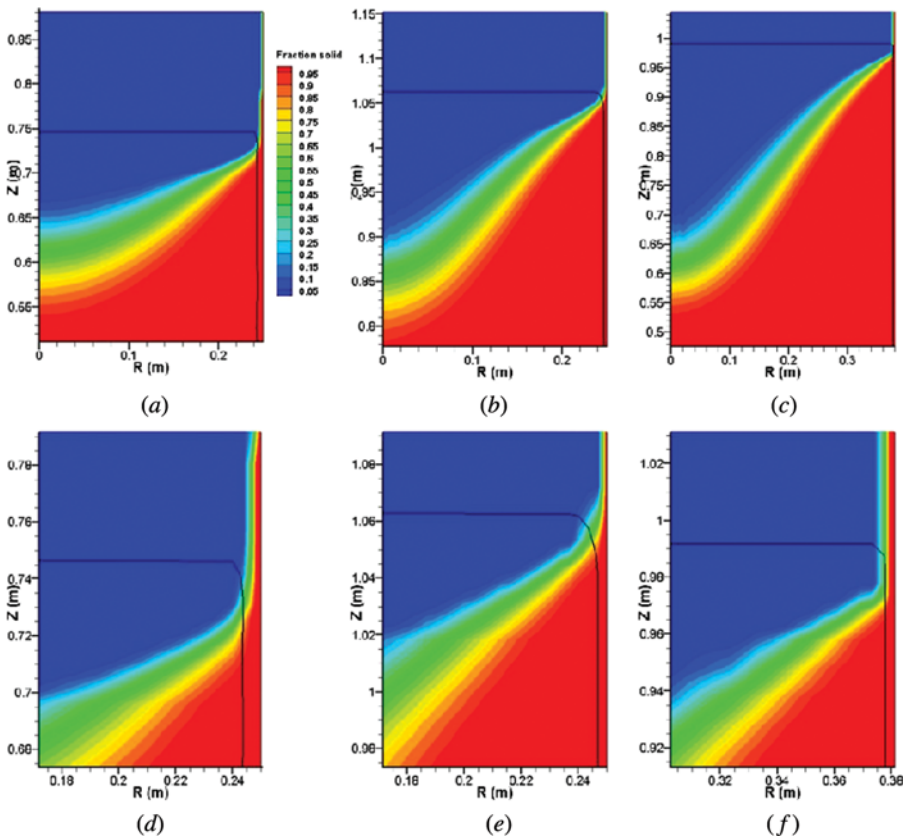


Figure 9. Comparison sump shape near the mold wall at 200 min for (a) Case 1, (b) Case 2 (increased current density), and (c) Case 3 (increased ingot radius). Close-up views of the slag skin thickness are shown for (d) Case 1, (e) Case 2, and (f) Case 3. The black lines indicate the slag–metal interfaces and shading the fraction solid field.

sumps with similar solidification front slopes. The sump depth at the centerline in Case 3 is double (28 cm) the sump depth in Case 2 because of Case 2's smaller diameter. At this point in the processes, most of the heat is leaving through the mold wall and the depth of the sump is controlled by the distance from the mold and how fast the ingot grows. The larger diameter case has a larger effective distance for heat to travel, leading to a deeper sump.

In Figure 10b, normalized sump depths are plotted as a function of the normalized radius for Cases 1–3. The calculated sump depths show stair-stepped increases in sump depth due to the coarseness of the numerical grid. In Case 1, the sump depth increases sharply near the outer radius, but flattens out near the midradius, giving a shallow, bowl-shaped sump. This shape is the result of the high heat transfer to the mold occurring at low filling velocities. As the filling velocity increases, Cases 2 and 3, there is less time for heat transfer to the mold wall and so the shape of the sump is elongated. The filling velocities in Figure 10a also show a general decrease over time, with Case 1 showing the fastest rate of decrease, even as the liquid sump and flow

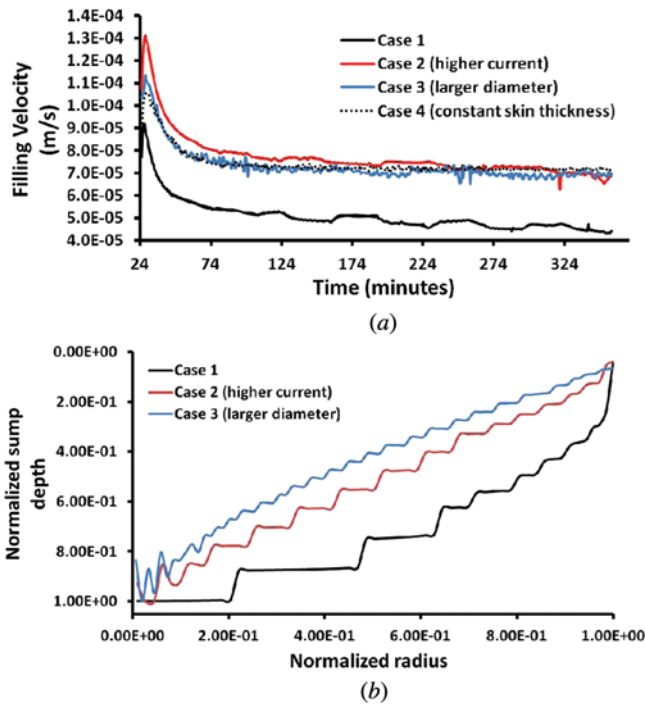


Figure 10. Comparison of different ESR runs. (a) Filling velocity histories for Cases 1–4. (b) Normalized sump depth as a function of the normalized radius for Cases 1–3 showing that sumps in Cases 2 and 3 are less curved than those in Case 1.

patterns are at steady state. The formation of a frozen slag skin on the mold reduces the amount of liquid slag available in the cap to generate heat. Case 1 exhibits a much thicker slag skin, which leads to a quicker reduction in slag cap thickness and so the filling velocity. The short-term variations in filling velocity in Figure 10a also show that Cases 1 and 2 seem to have similar amplitude variations in filling velocity, where Case 3 shows higher frequency and amplitude variations. These variations are due to changing flow patterns in the slag cap even during constant current operation.

5.3. Effect of Including Slag Skin Variation in Model

In the last case examined, the phenomenon of transient slag freezing is removed. Instead of forming a (possibly nonuniform) slag skin at the mold wall, which gives a thermal resistance as a function of the process behavior and thins the slag cap, the thermal resistance of a fixed skin layer thickness is combined with the heat transfer coefficient between the cooling water and the mold wall. This effective heat transfer coefficient assumes a uniform 3 mm skin, which is a few millimeters below the thickness predicted by Case 1 at the bottom of the slag cap, but about twice the thickness predicted in the top two-thirds of that cap. The effect of this variation in slag skin on filling velocity is shown in Figure 9, which shows that this change in thermal

resistance due to different treatments of slag skin causes the filling velocity in Case 4 to be almost twice that for the variable skin in Case 1. Case 4 also exhibits the high-frequency, low-amplitude variations in filling velocity of Cases 1–3, but it does not show a gradual decrease in filling velocity because the slag cap remains at a constant thickness.

All of the results in this study assume that the only resistances to heat transfer from liquid slag to mold are the presence of slag skin and the heat transfer through the mold, ignoring any effect of a contact resistance between the solidifying slag and any air gap there due to solidification shrinkage in the slag cap. The results presented thereby amplify the sensitivity of the melt rate and sump shape to treatment of the slag skin. Another large influence on these results is the thermal conductivity and porosity of the slag skin, which is not well characterized, especially at the high temperatures in question. However, while these uncertainties may change the level of sensitivity, the general trends shown here should be valid.

6. CONCLUSIONS

A numerical model has been presented that successfully modifies and integrates existing VOF techniques into a continuum mixture model for fluid flow, heat and mass transfer, solidification, and electromagnetics. This transport model with VOF has been validated against experimental results and applied to electroslag remelting, an important secondary ingot production process. Using the VOF technique allows the direct simulation of slag skin freezing to the mold, and this model has shown how including this variable slag skin thickness affects melt rate and sump shapes in ESR. It also highlights the melt rate differences when assuming a constant slag skin thickness compared with coupling the slag skin thickness to process behavior.

FUNDING

Portions of this research were funded by the National Science Foundation (CMMI-0456534 and CMMI-0900624). Funding for Mr. Fezi was provided by Precision Castparts Corporation.

REFERENCES

1. M. J. M. Krane, M. Fahrman, J. Yanke, E. Escobar de Obaldia, K. Fezi, and J. Busch, A Comparison of Predictions of Transport Phenomena in Electroslag Remelting to Industrial Data 2011, *Proc. Int. Symp. Liquid Metal Processing and Casting*, Nancy, France, pp. 65–72, 2011.
2. J. D. Busch, J. J. deBarbadillo, and M. J. M. Krane, Flux Entrapment and Titanium Nitride Defects in Electroslag Remelting of Incoloy Alloys 800 and 825. *Met. Mater. Trans. A*, vol. 44A, pp. 5295–5303, 2013.
3. A. H. Dilwari and J. Szekely, A Mathematical Model of Slag and Metal Flow in the ESR Process, *Met. Trans. B*, vol. 8B, pp. 227–236, 1977.
4. A. H. Dilwari and J. Szekely, Heat Transfer and Fluid Flow Phenomena in Electroslag Refining, *Met. Trans. B*, vol. 9B, pp. 77–87, 1978.

5. M. Choudhary and J. Szekely, The Modeling of Pool Profiles, Temperature Profiles and Velocity Fields in ESR Systems, *Met. Trans. B*, vol. 11B, pp. 439–453, 1980.
6. M. Choudhary and J. Szekely, Modeling of Fluid Flow and Heat Transfer in Industrial-Scale ESR System, *Ironmaking Steelmaking*, vol. 8, pp. 225–232, 1981.
7. M. Choudhary, J. Szekely, B. I. Medovar, and Y. G. Emelyanenko, The Velocity Field in the Molten Slag Region of ESR Systems: A Comparison of Measurements in a Model System with Theoretical Predictions, *Met. Trans B*, vol. 13B, pp. 35–43, 1982.
8. Y. M. Ferng, C. C. Chieng, and C. Pan, Numerical Simulations of Electro-Slag Remelting Process, *Numer. Heat Trans. A*, vol. 16, pp. 429–449, 1989.
9. M. H. Hsieh, C. L. Lai, and S. S. Lian, Numerical Simulation of Electroslag Remelting Process, *J. Chin. Soc. Mech. Eng.*, vol. 11, pp. 217–232, 1990.
10. L. A. Bertram, P. R. Schunk, S. N. Kempka, F. Spadafora, and R. Minisandram, The Macroscale Simulation of Remelting Processes, *JOM*, vol. 50, pp. 18–21, 1998.
11. K. M. Kelkar, S. V. Patankar, and A. Mitchell, Computational Modeling of the Electroslag Remelting (ESR) Process Used for the Production of Ingots of High-Performance Alloys 2005, *Proc. Int. Symp. Liquid Metal Processing and Casting*, Santa Fe, NM, pp. 137–144, 2005.
12. A. D. Patel and K. M. Kelkar, New Insights into the Electro-Slag Remelting Process Using Mathematical Modeling 2009, *Proc. MCWASP-XII*, Vancouver, BC, pp. 69–76, 2009.
13. V. Weber, A. Jardy, B. Dussoubs, D. Ablitzer, S. Rybéron, V. Schmitt, S. Hans, and H. Poisson, A Comprehensive Model of the Electroslag Remelting Process: Description and Validation, *Met. Mater. Trans. B*, vol. 40B, pp. 271–280, 2009.
14. V. Weber, Simulation numérique du procédé de refusion sous latier électroconducteur, Ph.D. dissertation, Institut National Polytechnique de Lorraine, Nancy, France, 2008.
15. A. Kharicha, W. Schützenhöfer, A. Ludwig, and G. Reiter, Influence of the Slag/Pool Interface on the Solidification in an Electro-Slag Remelting Process, *Mater. Sci. Forum*, vol. 649, pp. 229–236, 2010.
16. A. Kharicha, A. Ludwig, and M. Wu, 3D Simulation of the Melting During an Industrial Scale Electro-Slag Remelting Process 2011, *Proc. Int. Symp. Liquid Metal Processing and Casting*, Nancy, France, pp. 41–48, 2011.
17. Y. K. Chae, J. Mostaghimi, and T. Yoshida, Deformation and Solidification Process of a Super-Cooled Droplet Impacting on the Substrate Under Plasma Spraying Conditions, *Sci. Technol. Adv. Mater.*, vol. 1, pp. 147–156, 2000.
18. C. W. Hirt and B. D. Nichols, Volume of Fluid (VOF) Method for the Dynamics of Free Boundaries, *J. Comp. Phys.*, vol. 39, pp. 201–225, 1981.
19. W. J. Rider and D. Kothe, Reconstructing Volume Tracking, *J. Comp. Phys.*, vol. 141, pp. 112–152, 1998.
20. S. H. Garrioch, A Volume Tracking Method for the Simulation of Two-Fluid Flows, Ph.D. dissertation, McGill University, Montreal, Quebec, Canada, 2000.
21. M. Rudman, A Volume-Tracking Method for Incompressible Multifluid Flows with Large Density Variations, *Int. J. Numer. Methods Fluids*, vol. 28, pp. 357–378, 1998.
22. M. S. Kim and W. I. Lee, A New VOF-Based Numerical Scheme for the Simulation of Fluid Flow with Free Surface. Part I: New Free Surface-Tracking Algorithm and its Verification, *Int. J. Numer. Methods Fluids*, vol. 42, pp. 765–790, 2003.
23. M. Malik, E. Fan, and M. Bussmann, Adaptive VOF with Curvature-Based Refinement, *Int. J. Numer. Methods Fluids*, vol. 55, pp. 693–712, 2007.
24. M. Raessi, J. Mostaghimi, and M. Bussmann, A Volume-of-Fluid Interfacial Flow Solver with Advected Normals, *Comp. Fluids*, vol. 39, pp. 1401–1410, 2010.
25. W. H. Press, S. A. Teukolsky, W. T. Vetterling, and B. P. Flannery, *Numerical Recipes in Fortran 77: The Art of Scientific Computing*, Cambridge University Press, New York, NY, 1986.

26. J. O'Rourke, *Computational Geometry in C*, 2nd ed., Cambridge University Press, Cambridge, UK, 1998.
27. S. H. Garrioch and B. R. Baliga, A PLIC Volume Tracking Method for the Simulation of Two-Fluid Flows, *Int. J. Numer. Methods Fluids*, vol. 52, pp. 1093–1134, 2006.
28. W. D. Bennon and F. P. Incropera, A Continuum Model for Momentum, Heat and Species Transport in Binary Solid-Liquid Phase Change Systems-I. Model formulation, *IJHMT*, vol. 30, pp. 2161–2170, 1987.
29. M. Davidson and M. Rudman, Volume-of-Fluid Calculation of Heat or Mass Transfer Across Deforming Interfaces in Two-Fluid Flow, *Numer. Heat Trans. B*, vol. 41, pp. 291–308, 2002.
30. S. V. Patankar, *Numerical Heat Transfer and Fluid Flow*, Hemisphere Publishing, Washington, DC, 1980.
31. M. Francois, S. Cummins, E. Dendy, D. Kothe, J. Sicilian, and M. Williams, A Balanced-Force Algorithm for Continuous and Sharp Surface Tension Models within a Volume Tracking Framework, *J. Comp. Phys.*, vol. 213, pp. 141–173, 2006.
32. W. D. Bennon and F. P. Incropera, Numerical Analysis of Binary Solid-Liquid Phase Change Using a Continuum Model, *Numer. Heat Trans.*, vol. 13, pp. 277–296, 1988.
33. J. C. Martin and W. J. Moyce, Part IV: An Experimental Study of the Collapse of Liquid Columns on a Rigid Horizontal Plane, *Philos. Trans. R. Soc. London, Ser. A*, vol. 244, pp. 312–324, 1952.
34. K. Shinoda, T. Koseki, and T. Yoshida, Influence of Impact Parameters of Zirconia Droplets on Splat Formation and Morphology in Plasma Spraying, *J. Appl. Phys.*, vol. 100, p. 74903, 2006.
35. J. Madjeski, Solidification of Droplets on a Cold Surface, *IJHMT*, vol. 19, pp. 1009–1013, 1976.
36. A. D. Patel, Analytical Model for Electromagnetic Fields in ESR and VAR Processes 2003, *Proc. Int. Symp. Liquid Metal Processing and Casting*, Nancy, France, pp. 205–214, 2003.
37. L. A. Bertram, R. S. Minisandram, and K.-O. Yu, Vacuum Arc Remelting and Electroslag Remelting, in K.-O. Yu (ed.), *Modeling for Casting and Solidification Processing*, pp. 565–612, CRC Press, Boca Raton, FL, 2002.